In vivo real-time imaging reveals megalin as the aminoglycoside gentamicin transporter into cochlea whose inhibition is otoprotective

Jinkyung Kim[a] and Anthony J. Ricci[a,b,1]

[a]Department of Otolaryngology, Stanford University School of Medicine, Stanford, CA 94305; and [b]Department of Molecular and Cellular Physiology, Stanford University School of Medicine, Stanford, CA 94305

Edited by Matthew Kelley, National Institute on Deafness and Other Communication Disorders, National Institutes of Health, Bethesda, MD; received September 29, 2021; accepted January 5, 2022 by Editorial Board Member Jeremy Nathans

Aminoglycosides (AGs) are commonly used antibiotics that cause deafness through the irreversible loss of cochlear sensory hair cells (HCs). How AGs enter the cochlea and then target HCs remains unresolved. Here, we performed time-lapse multicellular imaging of cochlea in live adult hearing mice via a chemo-mechanical cochleostomy. The in vivo tracking revealed that systemically administered Texas Red–labeled gentamicin (GTTR) enters the cochlea via the stria vascularis and then HCs selectively. GTTR uptake into HCs was completely abolished in transmembrane channel-like protein 1 (TMC1) knockout mice, indicating mechanotransducer channel-dependent AG uptake. Blockage of megalin, the candidate AG transporter in the stria vascularis, by binding competitor cilastatin prevented GTTR accumulation in HCs. Furthermore, cilastatin treatment markedly reduced AG-induced HC degeneration and hearing loss in vivo. Together, our in vivo real-time tracking of megalin-dependent AG transport across the blood–labyrinth barrier identifies new therapeutic targets for preventing AG-induced ototoxicity.

in vivo cochlear imaging | drug tracking | aminoglycoside | ototoxicity | megalin

Drug-induced ototoxicity is a major side effect of several pharmacological treatments for life-threatening diseases (1). Aminoglycosides (AGs) which are widely used antibiotics, are one of the most common ototoxic drugs in clinical use (2). To treat severe Gram-negative infections, sepsis and, tuberculosis (3), over 10 million annual doses of AG are used in the United States (4). In some developing countries, AGs are used as a first line treatment owing to their broad-spectrum efficacy, a low incidence of allergic reactions, and limited antibiotic resistance (3, 4). Nevertheless, AGs can cause irreversible hearing loss by inducing selective degeneration of cochlear sensory hair cells (HCs) (5).

The cochlea is composed of three fluid-filled chambers, the scala vestibuli (SV), the scala media (SM), and the scala tympani (ST) (Fig. 1*A*) (6). SM is comprised of a high K^+/low Ca^{2+} endolymph solution, while SV and ST are filled with a perilymph solution having a similar ionic composition as extracellular fluid (7, 8). The unique endolymph ionic composition is maintained by the stria vascularis, where the blood–labyrinth barrier is presumably housed. Dense blood vessels and multiple transporters in the cells of the stria vascularis selectively regulate ion transport to the endolymph (9, 10). HCs that are in the organ of Corti (OoC) lie on the basilar membrane separating the SM and ST. More specifically, HC stereocilia which include mechanotransducer (MET) channels are exposed to the endolymph in SM, while the cell body is exposed to the perilymph (11–13).

Several possible mechanisms of AG transport into the cochlea and HCs have been proposed. AG entry into endolymph via the stria vascularis is reported based on localization of gentamicin-conjugated Texas Red (GTTR) (14, 15) or AG immunolabeling (16). Reissner's and basilar membranes have also been considered as possible entry routes of AG into the endolymph (17), but trafficking across the strial blood–endolymph barrier predominates compared to the uptake from perilymph (18). Despite the convergence of information supporting AG transport across the stria vascularis into endolymph, the molecular mechanism for transport remains unknown. In vitro assays using neonatal cochlea tissue demonstrated that MET channels are the main mediator of AG entry into HCs from the endolymph (19–22). Whether this remains true in adult in vivo conditions needs to be determined (21, 23). Modified AGs that show less permeation through the MET are also less toxic in vivo (24). Other routes like transient receptor potential (TRP) channels (25, 26), endocytosis (27), and purinergic receptors (28) may also contribute to HC uptake. However, the state of these routes under in vivo conditions and whether their participation occurs under normal or pathophysiological states is unknown. Regardless, these channels have a large pore, MET (1.3 nm) (20, 29), TRPA1 (~1.1–1.4 nm) (30), and TRPV1 (~1 nm) (31) in common, which supports an argument for direct permeation of AG (0.8–0.9 nm) (20, 32) into the cells. Possible therapeutic targets for preventing AG ototoxicity also have been explored by blocking one of the AG transport pathways or intracellular mechanisms (32, 33). For example, MET channel blockers (34–36) as well as antioxidants and anti-apoptotic agents were proposed with some limited efficacy (37–39).

Significance

Ototoxicity is a major side effect of aminoglycoside (AG) antibiotics; however, the mechanism by which this drug enters the cochlea and target hair cells (HCs) is not fully understood. Here, we developed an in vivo cochlear imaging method that enables real-time tracking of ototoxic drug transport into the cochlea in hearing adult mice. The time-lapse monitoring of drugs identified megalin as the major transporter of AG into the endolymph and the mechano-transducer channels as the portal into the HCs. Blocking megalin in vivo prevents AG-induced ototoxicity. Therefore, this study identifies an AG uptake pathway into the cochlea and provides a therapeutic target to eliminate drug-induced hearing loss.

Author contributions: J.K. and A.J.R. designed research; J.K. performed research; J.K. contributed new reagents/analytic tools; J.K. analyzed data; J.K. and A.J.R. wrote the paper; and A.J.R. supervised the entire project.

The authors declare no competing interest.

This article is a PNAS Direct Submission. M.K. is a guest editor invited by the Editorial Board.

[1]To whom correspondence may be addressed. Email: aricci@stanford.edu.

This article contains supporting information online at http://www.pnas.org/lookup/suppl/doi:10.1073/pnas.2117946119/-/DCSupplemental.

Published February 23, 2022.

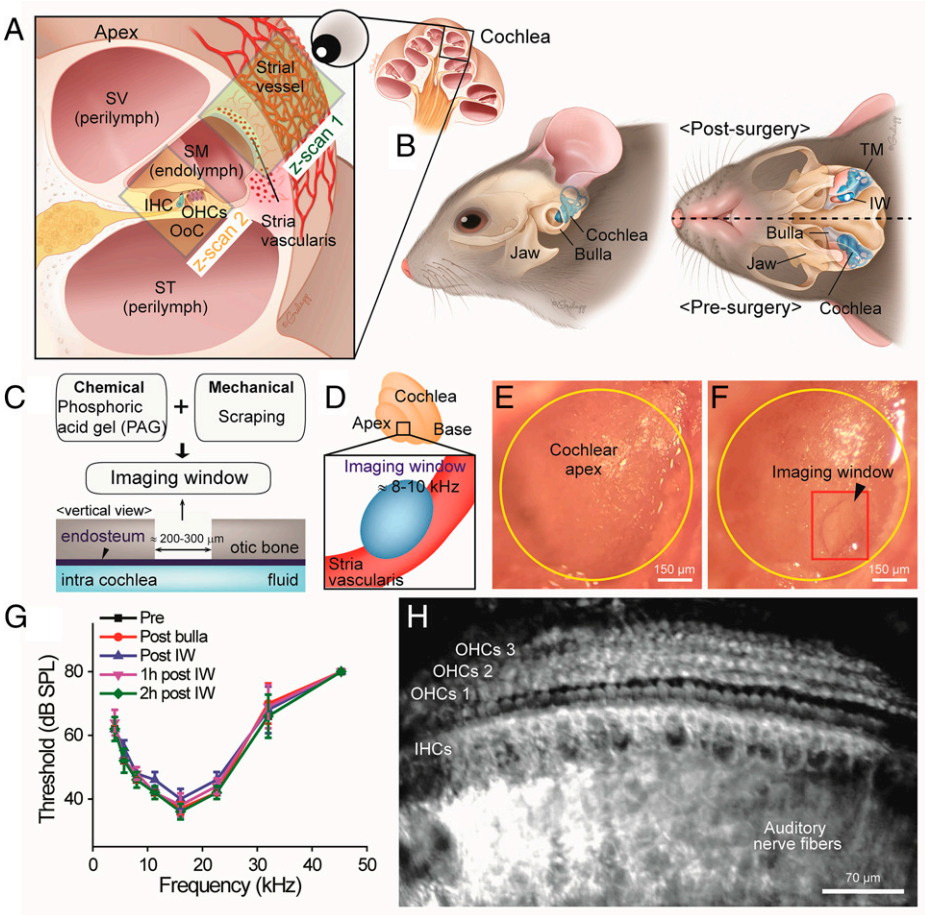

Fig. 1. Surgical approach for generating an IW for in vivo imaging of cochlear cells with preserved hearing function. (*A*) Illustrations of cochlea show three fluid-filled chambers (SV, SM, and ST), OoC, and stria vascularis. Eye ball indicates the direction of imaging path. The range of two z-scans are demonstrated by green (z-scan1, stria vascularis region, 100 μm depth) and yellow (z-scan 2, OoC region, 60 μm depth) boxes. (*B*) Illustrations of cochlea within a mouse are shown to provide orientation; *Left*, side view; *Right*, transverse view. In the transverse view, the mouse head was divided to display pre- and post-surgical conditions. Post-surgery image shows the bulla opening with a preserved tympanic membrane and an IW (white circle). Schematics of (*C*) the CMC for preventing intracochlear fluid leakage during IW formation and (*D*) the position of the IW. Note that the cochlear endosteum (dark blue) remains intact after IW formation, thus avoiding intracochlear fluid leaking. Cochlear apex images (*E*) before and (*F*) after IW formation (red box and black arrowhead) with a diameter of ~200–300 μm. Yellow circle indicates cochlea. The IW is near the 8–10 kHz region (43). (*G*) ABR thresholds were obtained after each surgical step and over time after IW formation with CMC ($n = 5$). ANOVA shows that no statistically significant differences were seen between comparisons ($P > 0.05$). (*H*) Representative two-photon in vivo image of the cochlear apex through the IW. AM1-43 dye (1 μL of 2.5 mM solution) was injected through the round window after intracochlear pressure release (by formation of a SCC hole) to visualize cells in the OoC. Note that the mouse lost its hearing after the dye injection.

Previous efforts to identify uptake pathways have primarily relied on in vitro assays using the immature, neonatal cochlea or fixed tissues from the mature cochlea, which have led to some conflicting results (14, 16). To overcome these limitations, we developed an in vivo multicellular cochlear imaging method in live, hearing adult animals. In vivo imaging of the cochlea at the cellular level is especially challenging (Fig. 1*B*) because: (i) the deep location within the temporal bone makes access difficult, (ii) the fluid-filled bony structure prevents imaging cells, and (iii) existing surgical approaches for in vivo studies cause hearing loss. We have overcome these obstacles by creating an imaging window (IW) on the otic capsule using a chemo-mechanical cochleostomy (CMC) that prevented intracochlear fluid leakage and hearing loss.

We used this surgical approach to track AG transport into cochlea and HCs in adult hearing animals in vivo in real-time. Systemically administered GTTR first appeared in the stria vascularis and later HCs in the OoC. We revealed that the major route of AG entry into HCs is via MET channels. We further demonstrated that entry into the endolymph is regulated by the endocytic transporter, megalin. Cilastatin, which inhibits the binding between megalin and AGs, significantly reduced HC uptake of GTTR and reduced AG-induced HC degeneration and hearing loss in vivo.

Results

An In Vivo Cochlear Imaging Method with a Preserved Hearing Function. We present a surgical and imaging approach that allows for intracochlear multicellular imaging from the functioning adult mouse cochlea. Historically, in vivo approaches are technically limited due to the anatomy and mechanosensitivity of the cochlea. We have overcome these obstacles by creating an IW on the otic capsule bone using a chemo-mechanical approach.

The bulla of an adult mouse was exposed and cochlear apex was accessed while preserving the tympanic membrane and other middle ear structures (*SI Appendix*, Fig. S1 *A–F*) (40, 41). The otic capsule bone of the entire cochlear apex was exposed after removing part of the bulla bone using a chemo-mechanical approach involving the application of phosphoric acid gel (PAG) (42) (*SI Appendix*, Fig. S1 *G* and *H*).

The endosteum (the thin membrane below the otic capsule bone, Fig. 1*C*) needs to be intact to prevent intracochlear fluid leakage while creating an IW. To ensure an intact endosteum, we reduced intracochlear pressure by creating a tiny hole on the posterior semicircular canal (SCC) (*SI Appendix*, Fig. S2 *A–C*). The reduced pressure separates the endosteum from the otic capsule bone, allowing us to avoid damaging the endosteum while creating an IW. This opening of the posterior SSC did not cause any detectable threshold shifts of the auditory brainstem responses (ABRs) (*SI Appendix*, Fig. S2*D*).

After reducing the intracochlear pressure, we again used a chemical (PAG) and mechanical (scraping) strategy to generate an IW through the otic capsule bone (Fig. 1*C*). PAG treatment was stopped when the surface of remaining bone was ∼80 μm away from endolymph as further reduction resulted in the highly acidic PAG accessing the intracochlear fluids, inducing ABR threshold shifts. An IW with a diameter of ∼200–300 μm (8–10 kHz region) (43) was created using a needle to slice through the thinned bone and peeling the remaining bone from the endosteum (Fig. 1 *D–F*). Note that a transparent IW similar to that used for brain imaging (10–30 μm thickness of the skull) (44) is not possible here, because the cochlear otic capsule bone with the 10–30 μm thickness fractures, leading to internal damage and ABR threshold shifts. Following IW formation, the posterior SCC hole was closed. Using this stepwise surgical approach resulted in no permanent ABR threshold shifts as assessed after each step (Fig. 1*G* and *SI Appendix*, Fig. S3*A*). More specifically, IW formation by CMC in the absence of fluid leakage from the cochlea induced a slight, transient threshold shift (3 ± 1 dB SPL) that was fully recovered within 2 h (Fig. 1*G*). Necessity of each surgical step was validated (*SI Appendix*, Note S1 and Fig. S2 *E–G*).

In Vivo Multicellular Image of Cochlea with Cellular Resolution. We used two-photon microscopy to ensure tissue penetration and to limit phototoxicity. Because we are sterically limited in accessing the IW without compromising the middle ear, we use a long working distance (19 mm) dry objective. A diagram of our two-photon system and the spatial/temporal resolutions obtained with this objective are described in *SI Appendix*, Figs. S4 and S5, respectively. With this system and mouse positioning (*SI Appendix*, Fig. S6), we resolved individual IHCs, OHCs, supporting cells (phalangeal, pillar, and border cells), and auditory nerve fibers (Fig. 1*H* and Movies S1 and S2 and *SI Appendix*, Fig. S3*B*), providing in vivo multicellular cochlear images with cellular resolution.

In Vivo Real-Time Monitoring of AG Uptake in Cochlea. To investigate AG trafficking routes into the cochlea, we performed two-photon in vivo cochlear imaging of GTTR (14) (*SI Appendix*, Fig. S3*C*). GTTR (100 mg/kg) was intraperitoneally injected (i.p.) into mice and in vivo images were acquired prior to and every 30 min after injection for up to 3 h total. The ABR was measured every hour. For in vivo imaging, we performed two z-stack scans, one for the stria vascularis region (z-scan 1: green box) and the other for the OoC (z-scan 2: yellow box), specifically the HC layer region (Fig. 1*A*). Different laser powers were used for each z-scan (15 mW for stria vascularis region and 40 mW for OoC region) because the intensity of GTTR fluorescence in the stria vascularis was much higher than that in HCs. The location of the IW is the 8–10 kHz region (43) of the cochlear apex (Fig. 1*D*), and the field of view (FOV) is shown in *SI Appendix*, Fig. S6*C*. In vivo z-projected images revealed the intensity of GTTR gradually increased over time in the stria vascularis (*SI Appendix*, Fig. S7*A*) and HC (*SI Appendix*, Fig. S7*B*) regions. The GTTR signal in stria vascularis initially appeared within 10 min after i.p. injection, indicating a rapid uptake of GTTR. Similar to stria vascularis, HCs uptake GTTR, but the uptake began later and accumulated more slowly than that in the stria vascularis. Even though our z-scan included all cell types within along the basilar membrane, HCs were the only cell type where we consistently detected GTTR uptake.

For quantification of GTTR intensity in the time-series images, a region of interest (ROI) which included either stria vascularis or basilar membrane was selected in the box (yellow box in *SI Appendix*, Fig. S8 *A* and *F*). We could not use the intensity from each strial vessel or HC for the quantification because the boundary was not clear at early time points. A z-projected image, instead of a single scan, was used for the quantification (*SI Appendix*, Fig. S8 *A*, *B*, *F*, and *G*). Each single scan only resolves a part of the structures because the cochlea does not lie flat in the imaging plane (*SI Appendix*, Fig. S8 *C–E* and *H–J*).

Intensity increments over time are described in *SI Appendix*, Fig. S7 *C* and *D*, showing gradual uptakes of AG from stria vascularis and HCs over time. In experiments with the i.p. injection of GTTR, a large variability in signal intensity in HCs was observed among individual animals. For example, two of five mice did not show GTTR signal in HCs within 3 h after the i.p. injection (mice 03 and 04 in *SI Appendix*, Fig. S7*D*). Furthermore, the time when the GTTR signal was initially detected varied between the mice that did show uptake (mice 01, 02, and 05 in *SI Appendix*, Fig. S7*D*).

To reduce the variability of uptake, we moved to intravenous (i.v.) injection of GTTR (10 mg/kg), which also reflects clinical use. A retro-orbital injection was adopted because it is easier than a general tail vein injection and both routes of injection were similarly effective (45). In contrast to i.p. injection, GTTR intensity in stria vascularis rapidly appeared right after i.v. injection and decreased over time (Fig. 2 *A–C* and *M*, *SI Appendix*, Fig. S9*A*, and Movie S3). This likely reflects the drug appearing as a bolus in the blood stream and slowly diluting and clearing from the blood. HCs quickly uptake GTTR in 10 min after the injection, and the intensity progressively increased over the ensuing 3 h (Fig. 2 *D–F* and *N*, *SI Appendix*, Fig. S9*B*, and Movie S4), indicating a gradual uptake of AG by HCs. ABR were measured pre- and post-surgery and while performing in vivo imaging (*SI Appendix*, Fig. S3*C*). A single i.v. injection of GTTR does not change hearing function (Fig. 2*O* and *SI Appendix*, Fig. S10*A*).

To confirm the uptake from HCs is specific to GTTR and not because of Texas Red dye, we injected the same concentration of Texas Red only (10 mg/kg) (*SI Appendix*, Fig. S11). The intensity of Texas Red rapidly appeared and then gradually reduced in stria vascularis similar to the results from GTTR injection (*SI Appendix*, Fig. S11*A*). However, there was no Texas Red signal in HCs (*SI Appendix*, Fig. S11 *B* and *C*). These data indicate that GTTR uptake into HCs is driven by the AG and not the dye. Note that the dye injection also did not change hearing function (*SI Appendix*, Fig. S10*B*).

MET Channel as an Entry Site of AG into HCs. Previous electrophysiological, molecular, and pharmacological measurements support an entry of AG into HC via MET channels (19–21), however, all data were acquired from the isolated neonatal tissues. To test for MET channel specificity of uptake in vivo, in adult animals, we used transmembrane channel-like protein 1 (TMC1) knockout (KO) mice which lacked MET channel function (21). In the mutant, a rapid increase followed by a gradual decrement of GTTR signal was detected in stria vascularis, similar to the wildtype cochlea (Fig. 2 *G–I* and *SI Appendix*, Fig. S9*C*). However, the signal was entirely absent in HCs, indicating that functional MET channels are critical for AG uptake into HCs (Fig. 2 *J–L* and *SI Appendix*, Fig. S9*D*). Note that

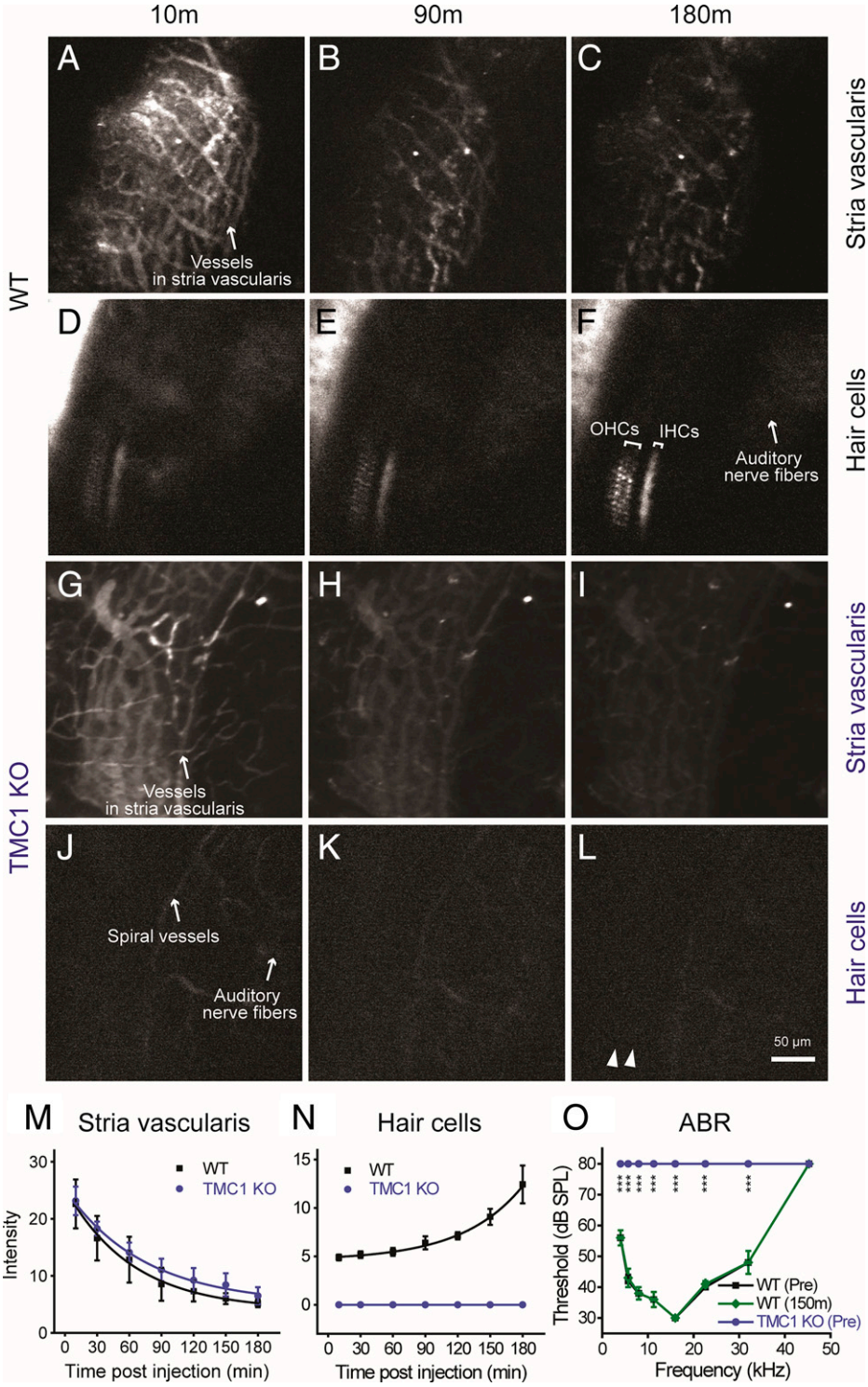

Fig. 2. In vivo time-lapse images of GTTR in control and TMC1 KO cochleae. (*A–F*) Two-photon z-projected images in wildtype mice. Images show GTTR uptake in stria vascularis of the cochlear apex (*A*) 10 min, (*B*) 90 min, and (*C*) 180 min after i.v. injection of GTTR. Images of OoC region show GTTR uptake from OHCs, IHCs, and nerve fibers (*D*) 10 min, (*E*) 90 min, and (*F*) 180 min after the injection. While the intensity of GTTR is gradually decreased over time in stria vascularis, it is increased in HCs. (*G–L*) Two-photon z-projected images in TMC1 KO mice. Images show GTTR uptake in stria vascularis (*G*) 10 min, (*H*) 90 min, and (*I*) 180 min after i.v. injection of GTTR. Images of OoC region show no uptake of GTTR in HCs (*J*) 10 min, (*K*) 90 min, and (*L*) 180 min after the injection. While a gradual decrement of GTTR signal is detected in the stria vascularis, there is no signal in the HCs. White arrow heads indicate the location where HCs are supposed to be placed. (*M*) Quantification of GTTR intensity shows a gradual decrement of the intensity over time from stria vascularis in both control and the mutant mice ($n = 5$ for each group). Changes of GTTR intensity over time fitted by exponential decay function were compared with f-test; $P < 0.001$. (*N*) Quantification of GTTR intensity shows that mutant HCs do not uptake GTTR whereas wildtype cells do ($n = 5$ for each group). $P < 0.001$, f-test. (*O*) ABR thresholds were obtained pre- and 150 min after GTTR injection in wildtype mice, and pre-injection in TMC1 KO ($n = 5$ for each group). The threshold in the mutant was measured only one time (pre-surgery) because they had no detected responses. ***$P < 0.001$, ANOVA and *t* test.

https://doi.org/10.1073/pnas.2117946119

HCs in the cochlear apex still remain at the age of TMC1 KO mice that we used for in vivo imaging (~4 wk), despite a progressive HC loss with age in the mutant (21, 46). There was no apoptotic signal in the mutant HCs, proven by TUNEL assay (*SI Appendix*, Fig. S12). Other possible defects, either directly due to additional TMC1 functions or downstream due to loss of MET responses, cannot be ruled out as potentially contributing to changes in AG uptake. Quantification showed a gradual decrement of GTTR intensity in stria vascularis over 3 h in both control and the mutant mice (Fig. 2*M*). In contrast to wildtype HCs, we did not detect any GTTR signals in HCs in the mutant mice over the 3 h imaging period (Fig. 2*N*). As expected, the mutant mice showed no ABR responses both pre- and post-injections (Fig. 2*O*). Together, these data provide in vivo observations that MET channels are required for AG uptake into cochlear HCs in adult mouse.

Megalin Is Required for AG Entry into Endolymph from Stria Vascularis. MET channels reside on HC stereocilia which protrude into the endolymphatic compartment (6). For MET channels to be accessible to AGs, the drugs must first cross the blood–labyrinth barrier and enter the endolymph. We hypothesized that megalin is required for AG entry into endolymph. Megalin, which is an endocytic receptor and a member of the low-density lipoprotein-receptor family, binds tightly to AGs and is found in both strial marginal cells and Reissner's membrane (47, 48). Furthermore, megalin is critical for AG transport in the kidney (49). Inhibiting the megalin receptor is nephroprotective (49). To inhibit the binding between megalin and AGs, we used cilastatin as a competitive antagonist. Cilastatin binds to megalin with a higher affinity than gentamicin, and it also does not inhibit the antibacterial activity of AGs (49).

Cilastatin (30 mg/kg) was i.v. injected immediately before i.v. injection of GTTR (10 mg/kg). In vivo time-lapse imaging demonstrated that the initial uptake of GTTR with a cotreatment of cilastatin in stria vascularis were very similar to the control group (Fig. 3 *A* and *G*). However, the GTTR remained in the stria vascularis for a longer time compared to GTTR only group (Fig. 3 *A–C* and *G* and *SI Appendix*, Fig. S13*A*). Even though HCs showed a small amount of initial GTTR uptake (Fig. 3*D*), there was no additional uptake over time with cilastatin treatment (Fig. 3 *D–F* and *H* and *SI Appendix*, Fig. S13*B*). These results suggest that cilastatin suppresses AG transport into endolymph. Our in vivo observation provides direct evidence that megalin is a major target site for AG entry from stria vascularis to endolymph and then HCs. As before, GTTR alone did not cause ABR threshold shifts and neither did cotreatment with cilastatin (Fig. 3*I* and *SI Appendix*, Fig. S10*C*).

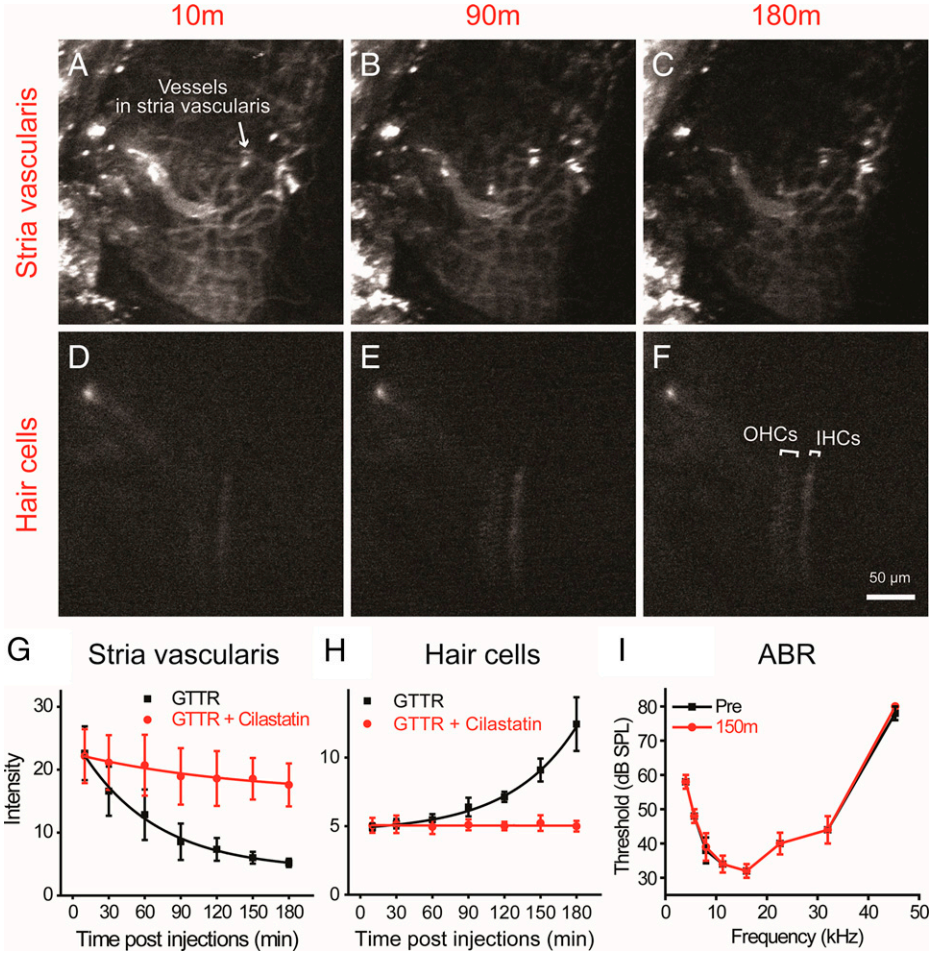

Fig. 3. In vivo time-lapse images of GTTR with co-administration of cilastatin. (*A–F*) Two-photon z-projected images show GTTR uptake in stria vascularis of the cochlear apex (*A*) 10 min, (*B*) 90 min, and (*C*) 180 min after i.v. injections of cilastatin and GTTR. The OoC region show GTTR uptakes from OHCs and IHCs (*D*) 10 min, (*E*) 90 min, and (*F*) 180 min after the injections. (*G* and *H*) Quantification of GTTR intensity shows less decrement of the GTTR signal in stria vascularis and almost no change in HCs over time compared to the control group ($n = 5$ for each group). Changes of GTTR intensity over time fitted by exponential decay function were compared with f-test; $P < 0.001$ in both plots. (*I*) ABR thresholds were obtained pre- and 150 min after cilastatin and GTTR injections ($n = 5$), and they were not statistically significantly different. $P > 0.05$, *t* test.

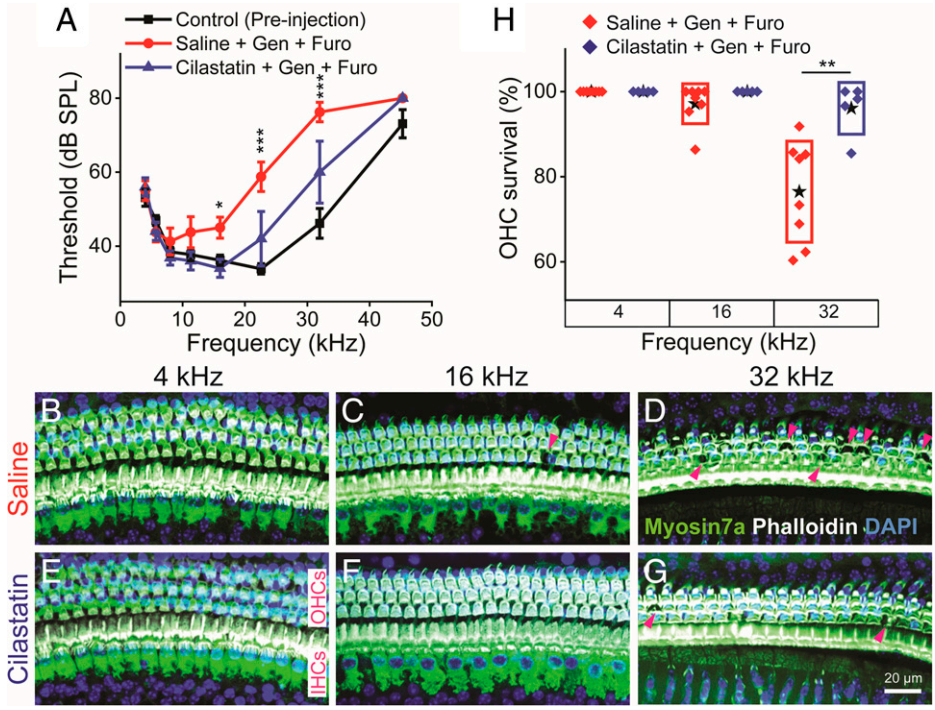

Fig. 4. Cilastatin protects against gentamicin-induced ototoxicity as measured from ABR thresholds and HC counts. (*A*) ABR thresholds were obtained pre- (n = 13) and 29 d after the i.p. injections of either "saline + gentamicin + furosemide" (n = 8) or "cilastatin + gentamicin + furosemide" (n = 5). (*B–G*) Representative confocal images of immuno-labeled whole mount cochleae, at 4, 16, and 32 kHz regions from the mice in *A*. Magenta arrow heads indicate the OHC loss. (*H*) OHCs at 4, 16, and 32 kHz cochlear regions were counted for comparison between the saline and the cilastatin group. More OHCs survived at 32 kHz in the cilastatin group than the saline group. *P < 0.05; **P < 0.01; ***P < 0.001, ANOVA and t test.

Blockage of Megalin by Cilastatin Prevents AG-Induced Ototoxicity. To evaluate whether cilastatin reduces AG-induced ototoxicity, we generated a multidose AG model using gentamicin and furosemide (50) (*SI Appendix*, Fig. S3*D*). Multiple i.p. injections are done within a day and continued for 10 d total. First, saline or cilastatin (360 mg/kg) was administrated to mice in each group. Thirty minutes later, we redosed with saline or cilastatin (180 mg/kg) followed by gentamicin (180 mg/kg). Last, furosemide (100 mg/kg) was applied 30 min after the gentamicin injection. Additionally, mice received saline or cilastatin (540 mg/kg) a day before starting the 10 d of injections.

ABRs were measured pre- and 29 d after the injection (Fig. 4*A*). The saline group (saline + gentamicin + furosemide) showed 9 to 30 dB ABR threshold elevations at 16, 22.6, and 32 kHz regions compared to pre-injection condition. However, the cilastatin group (cilastatin + gentamicin + furosemide) showed no significant change across frequencies in ABR thresholds. Consistent with the ABR result, immunolabeling showed that OHC survival rate in cochlear base in the saline group is significantly worse than that in the cilastatin group (Fig. 4 *B–G*). At 32 kHz region, while 96 ± 3% of OHC are survived in cilastatin group, only 76.5 ± 4.2% remains in saline group (P < 0.01, Fig. 4*H*). There was no IHC loss in either group. These results indicate that cilastatin-mediated inhibition of the megalin receptor greatly reduced AG-induced ototoxicity.

Discussion

As many as 20% of patients suffer from an irreversible hearing deficit as a side effect of AG treatment (51, 52). To find a therapeutic target to eliminate the ototoxic side effect, we need a clear understanding of how AGs enter the cochlea and how they target HCs. Here, we present an in vivo method to directly monitor AG uptake into the cochlea and HCs in real-time. The CMC surgical approach coupled with two-photon time-lapse imaging of GTTR reveals that AGs enter into endolymph via megalin receptors and into HCs via MET channels (Fig. 5). AG transport into endolymph is suppressed by the megalin antagonist, cilastatin (Fig. 3). Suppression of AG entry into endolymph by cilastatin protects against HC loss and auditory dysfunction (Fig. 4). These data provide important insight into AG-induced ototoxicity using in vivo real-time observation of ototoxic drug transport into the cochlea, identifying a role for megalin in transport, and demonstrating otoprotection by preventing AG transport into endolymph.

In vivo functional investigations of the cochlea remain challenging, owing to its deep location, mechanosensitivity and the fluid-filled, bone-encased nature of its structure. Previous in vivo cochlear studies such as laser Doppler velocimetry (53, 54), scanning laser interferometry (55, 56), or dual sensor (57) experiments provide the mechanical and/or electrical responses of a part of the organ of Corti to sound stimulation but lack cellular resolution. Other studies such as direct HC recordings (58, 59) or single unit recordings (60) provide individual cell functional responses, but no population information. These approaches are physically invasive and can impair cochlear function. Optical coherence tomography noninvasively probes cochlear motion with subnanoscale resolution but is still limited spatially (theoretically ~10 μm) and does not provide a cellular functional readout (40, 61, 62).

Our surgical approach overcomes these hurdles and allows us to resolve cochlear cells through an IW while preserving hearing function. A key aspect of the CMC method is maintaining an intact endosteum to avoid intracochlear fluid leakage. Since the endosteum is a thin membrane close to the bony otic capsule, it is inevitably damaged during most other cochleostomy procedures. Damage to the endosteum leads to the loss of intra cochlear fluid and pressure, resulting in immediate hearing loss. The CMC approach maintained the endosteum,

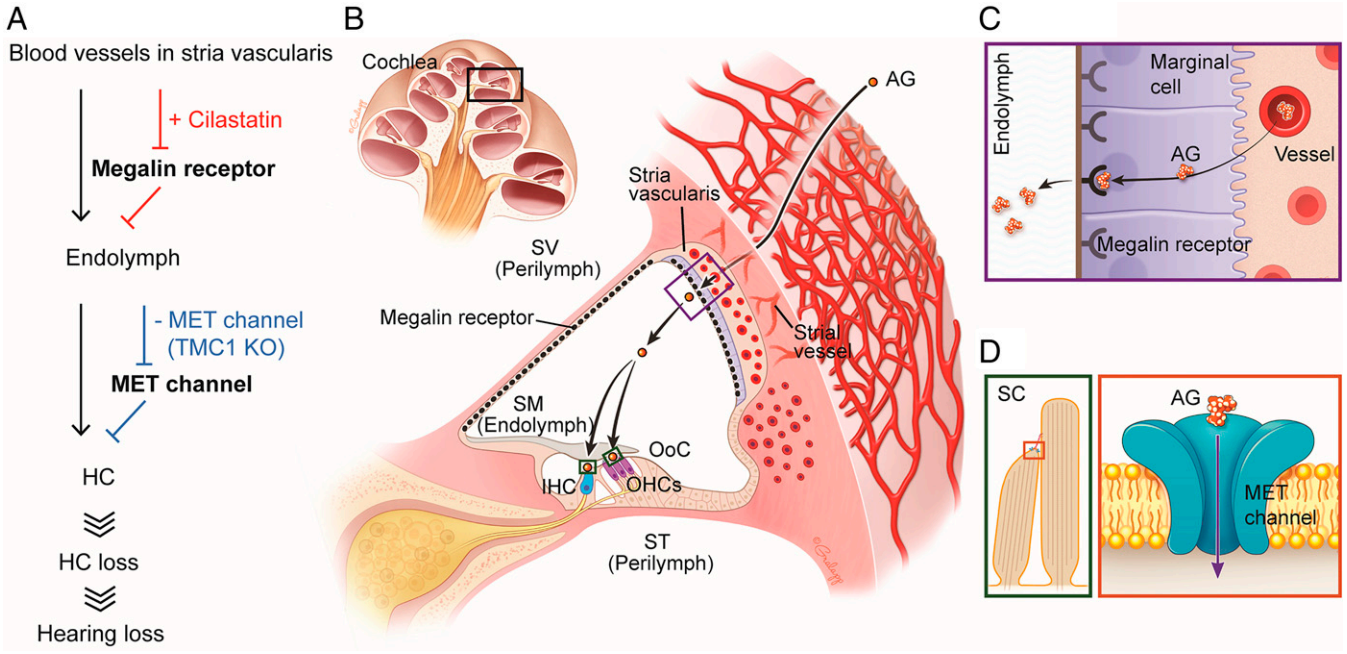

Fig. 5. AG entry route into cochlea and HCs. (*A*) Flowchart reveals AG transport into the cochlea via megalin and HCs via MET channels. (*B*) Illustration demonstrates distribution of megalin receptor (black dotted line) in the cochlea and AGs uptake route into cochlea and HCs. (*C*) Zoomed-in image of purple box in *A* provides the pathway of AGs into endolymph via megalin. (*D*) Zoomed-in images of green and orange boxes in *B* and *D* provide the pathway of AGs into HCs via MET channels.

while short-term intracochlear pressure release helped to separate the endosteum from the bone during the critical step of IW formation. Resealing the SCC hole allowed for pressure restoration and maintenance of hearing sensitivity. Importantly, this technique likely preserved MET channel and the electrochemical composition of the endolymph, both of which govern AG entry into HCs. Our innovative in vivo method established what we believe may be new avenues for investigation of physiological and pathophysiological questions regarding cochlear function. It also has potential translational implications as it may provide a new tool for drug delivery or diagnostic testing.

While prior studies have implicated MET channels as necessary for AG entry into HCs, whether this occurs in vivo and how AGs first enter the cochlea was unclear. Our data provide conclusive evidence that megalin is a critical component of AG transport into endolymph and AGs are targeted to HCs through MET channel entry. We and others have shown that AG ototoxicity can be effectively reduced by preventing AG uptake into the HCs (34–36, 63). Multiple sites of action of AGs can be targets for ototoxicity, and many of them overlap with antimicrobial targeting, making it difficult to eliminate ototoxicity without altering antimicrobial activity (17). Furthermore, AGs are not metabolized within HCs and potential therapies might need to be long term in order to prevent a slow deterioration (64). There is, however, a growing consensus that the main entry sites into HCs are the MET channels (19, 20). Here, we directly monitor uptake of AGs into HCs via MET channels in adult mice in real-time in vivo. The lack of signal in the TMC1 KO mouse shows specificity to the MET channel. Additionally, the 3 h time course of imaging should provide ample time for other transport mechanisms to be revealed. At first take, it is surprising that there is no change in ABR response during the uptake of GTTR when the GTTR would be predicted to block the MET channel. However, the hair bundle membrane potential is quite negative due to the endocochlear potential, endolymph has a very low Ca^{2+} concentration, and the amount of GTTR entering the endolymph is quite low; each of these factors likely leads to an alleviation of the channel block and promotion of permeation through the MET channel (29, 65, 66). Thus, if the channel is not blocked, ABRs will be unaffected.

Recent data also suggest that AGs enter other cells (14, 16). Under pseudo in vivo conditions (i.e., tissue is fixed and processed post-injection), AGs are detected in non-HCs where it is argued that, in living cells, the GTTR signal is masked in all but HCs, fixation unmasks the signal in other cell types. Neither present data nor previous data directly address the possibility of masking or the alternative hypothesis that GTTR diffuses across cells in fixed tissue. However, our data demonstrate that HC accumulation of AGs is required for toxicity, uptake via MET channels is the major entry pathway, and megalin receptors are the major transport mechanism into endolymph. HCs, not supporting cells, are the site of action for AGs. Blockage of entry via either of these two pathways reduces ototoxicity. Thus, the significance of other potential pathways into HCs or the ability of AGs to enter other cell types is greatly reduced because there is no evidence of functional relevance for these alternatives. Potentially, influx is reduced in cells without permeable ion channels and possibly efflux is enhanced so that AGs are not toxic in supporting cells.

Recent data also suggest that alternative means of HC entry exist under conditions that mimic sepsis (67), so future work is needed to provide measurements of uptake under these conditions. Whether MET channels are the only means of HC entry is less relevant than the data demonstrating that reducing entry into HCs by blocking passage through MET channels is otoprotective. Our technology allows this important question to be directly addressed.

Because MET channels are only located on HC stereocilia which project into the endolymph compartment, the question becomes, how do AGs enter the endolymph space in the first place? Megalin receptors are prime candidates because they regulate AG uptake in kidney and are found in strial marginal cells, as well as dark cells of the vestibular system and in the

cells comprising Reissner's membrane (47–49). Our data demonstrate a critical role for these transporters by blocking activity using cilastatin. The reduced clearance from the strial vasculature supports the conclusion that cilastatin blocks megalin receptors in the kidney, thus prolonging AG presence in the blood stream.

Cilastatin prevented the accumulation of AGs in HCs by blocking AG transport into endolymph. The initial HC labeling may represent a competition for binding to the megalin receptor (49). We assume that the initial high concentration of AG induced by i.v. bolus injection outcompetes cilastatin. However, later with AG dilution in the blood stream, cilastatin outcompetes the AG to prevent further accumulation. This idea is supported by previous work where binding was assayed using a quartz crystal microbalance analysis and initially AGs outcompeted megalin (49). Future work could lower the rate of i.v. delivery to prevent the initial accumulation of AGs. Hereto, sepsis conditions have suggested that alternative transport mechanisms arise across the strial tissue, and our technology will allow for direct analysis of this possibility. That megalin both prevents GTTR entry into HCs (Fig. 3) and is otoprotective (Fig. 4) supports the conclusion that drug modification (addition of Texas Red) does not alter the entry pathway. Although alternative mechanisms may be relevant, that megalin block is otoprotective is an exciting finding that provides a new target for further drug development.

Another important finding of our work is that the mode of delivery of the AGs greatly influences the pharmacokinetics of the drug. Intraperitoneal delivery slows transport to the vasculature and then uptake into HCs, however the accumulation within the vasculature is quite slow and variable (*SI Appendix*, Fig. S7*C*). In contrast, i.v. delivery provides a consistent and rapid accumulation in the strial vasculature which peaks prior to our initial imaging period (~10 min post-injection) and then decreases during the subsequent 3 h recording period (Fig. 2*M*). The differential uptake in the cochlea after i.p. and i.v. injections (*SI Appendix*, Fig. S7 *C*, *Right Panel*) may have important implications on existing AG ototoxicity models as many use i.p. injections, whereas AGs are administered i.v. in patient care. Thus, our data may guide future studies that model human AG ototoxicity.

Finally, we developed a multidose ototoxicity assay using gentamicin and furosemide that demonstrated cilastatin treatment was otoprotective. The model generated a moderate amount of HC loss and ABR threshold shifts that were both significantly reduced by cilastatin. It is well known that an induction of hearing loss in vivo with AGs in adult mice is remarkably difficult, unlike other larger mammals such as guinea pigs. Here, we induced hearing loss with coinjections of furosemide and gentamicin for 10 d. Cilastatin or saline was also treated to elucidate the role of megalin in AG trafficking to cochlea. Our ABR and immunolabeling results showed that cilastatin partially prevents HC and hearing loss (Fig. 4 *A* and *H*). We cannot rule out that furosemide triggers another mechanism of AG uptake from the cochlea and HCs. Additional uptake routes which furosemide might trigger is a blood–labyrinth barrier change in stria vascularis. Transient ischemia induced by furosemide temporarily disrupts the barrier, allowing the entry of toxic chemicals (50). A second possible route is via TRPV4 channels in stria vascularis and HCs. Osmotic swelling induced by inhibition of Na-K-2Cl cotransporter from furosemide application activates TRPV4 channels located in the stria vascularis, permitting AG entry through the channel (32). Furthermore, the low Ca^{2+} condition in endolymph may accelerate AG entry through the furosemide-activated TRPV4 channels in HCs and marginal cells in the stria vascularis (32). While this study did not investigate the mechanisms triggered by furosemide in depth, how furosemide and other mechanisms such as sepsis regulate the blood–labyrinth barrier are important directions to further characterize. It is also likely that dose and delivery timing of cilastatin could be modified as a means of enhancing otoprotection. We believe that our in vivo method can provide a better understanding of AG-induced ototoxicity. Regardless of the potential additional effects that might be induced by furosemide, cilastatin provided protection from AG toxicity and thus identifies megalin as a promising new target site.

In conclusion, we present an imaging method to investigate in vivo cochlear physiology and pathology in real-time. With this method, we provide in vivo confirmation that MET channels are the site of HC entry for AGs. We further dissected the AG entry pathway at the stria vascularis and identified megalin as a required transporter. Finally, in an AG-ototoxicity model, we have shown that blocking megalin transport greatly reduces AG-induced ototoxicity, opening a new therapeutic strategy to prevent hearing loss.

Materials and Methods

Animals. All studies were carried out according to the protocols approved by the Institutional Animal Care and Use Committee at Stanford University (APLAC-14345). We used C57BL/6 (Charles River: 026) and TMC1 KO (JAX: 019146) mice. Note that hybrid mice of C57BL/6 and FVB (Charles River: 027) were used for ABR measurements in *SI Appendix*, Fig. S2 *E–G*. Mice of either sex, between 4 and 8 wk of age were used. Mice were anesthetized using ketamine (100 mg/kg) and xylazine (10 mg/kg). After 1 h, supplemental anesthetic (25% of initial dose) was injected every 30 min. Anesthesia level was assessed by signs of movement or withdrawal reflex before the application of supplemental anesthetic.

Mouse Surgery. The surgical procedure was performed under a stereo microscope (SZ61, Olympus) with 20× eyepiece (WHSZ20X, Olympus). Under anesthesia, the mouse skull was exposed and attached to a custom-made head holder with dental glue (Teets Denture Material, Cooralite Dental Mfg. Co.) (*SI Appendix*, Fig. S1*A*). The mouse was flipped so the lower jaw faced upward to allow accessing of the cochlea from below while preserving the tympanic membrane and other middle ear structures. We surgically removed the skin and opened the bulla in the left ear after treatment with applied PAG (1 min, Etching gel, Young) to soften the bone and to access the apical cochlea turn without disturbing the tympanic membrane (*SI Appendix*, Fig. S1 *B–G*). Part of bulla bone (violet in *SI Appendix*, Fig. S1*G*) was softened with PAG application and removed with a needle (30Gx1/2, BD) to expose the otic capsule bone with the underlying stria vascularis (*SI Appendix*, Fig. S1*H*). PAG application helped to avoid mechanical stress on the bulla that can induce hearing loss through middle ear misalignment. The posterior and lateral SCCs were exposed next and opened to release intracochlear pressure (*SI Appendix*, Fig. S2*A*). PAG was applied for 1 min to the posterior SCC followed by making the hole with a needle (*SI Appendix*, Fig. S2 *B* and *C*). After the hole formation, we returned to the cochlear region. For IW formation, we applied PAG to the otic capsule bone for 10 to 20 s, followed by scraping it with a needle. The CMC was repeated one or two times depending on the thickness of the cochlear otic capsule bone. Before IW formation, the cochlear bone was cleaned with 1× phosphate-buffered saline (PBS). The IW was formed without disturbing the cochlear endosteum on the boundary of the stria vascularis (Fig. 1 *D–F*). The IW location was near the ~8–10 kHz region (43) and its diameter is ~200–300 μm. The key to a successful surgery is maintenance of the endosteum, which can be easily ripped when only using a mechanical approach, leading a large leak of intracochlear fluid (*SI Appendix*, Fig. S2*G*). After IW formation, we closed the hole in the SCC using a muscle plug and cyanoacrylate glue (Instant adhesive 101, Permabond). This surgery took ~1 h.

Drug Administration. GTTR was generated and purified, as previously described (14). Gentamicin (LE1046, Accel Pharmtech) was mixed with Texas Red succinimidyl esters (T20175, Invitrogen). The conjugate was separated from unconjugated gentamicin and unreacted Texas Red by C-18 column based reversed-phase chromatography. Soluble Texas Red was used as a control (S7635, Sigma-Aldrich). To block megalin receptors, cilastatin (C5743, Sigma-Aldrich) was applied. 1× PBS was used for the vehicle.

For in vivo imaging, GTTR or Texas Red was i.p. (100 mg/kg) or i.v. (10 mg/kg) injected into mice. Intravenous injection of 30 mg/kg cilastatin was followed by a single injection of GTTR (i.v. 10 mg/kg).

For investigations of otoprotection from cilastatin, either saline or cilastatin (360 mg/kg) was systematically administrated with i.p. injection. After 30 min, either saline or cilastatin (180 mg/kg) i.p. injection was followed by gentamicin i.p. injection (180 mg/kg). After another 30 min, both groups received a furosemide i.p. injection (100 mg/kg). These injections were repeated daily for 10 d. Note that either cilastatin (540 mg/kg) or saline i.p. injection was preceded 1 d before starting the injections as a pretreatment.

ABR Measurement. Under anesthesia, ABR potentials were recorded with a TDT system (System 3 RZ6, Tucker-Davis Technologies) using 3 stainless steel electrodes positioned in the vertex of the skull (+), the ventral surface of the tympanic bulla (−), and the hind leg (ground) (*SI Appendix*, Fig. S6*A*). The stimulus had a 5 ms duration and 0.2 ms gate time. The frequency range was 4 to 46.1 kHz, and the intensity range was from 10 to 80 dB SPL (10 dB SPL steps). A total of 512 responses were sampled and averaged at each sound level. The major peaks in ABR waveforms were tracked as a function of the intensity, and the lowest intensity level at which peaks were clear was determined to be the threshold. For the purpose of averaging, we set the threshold to 80 dB SPL when ABR peaks were not detected at or below 80 dB SPL.

Two-Photon In Vivo Imaging and Quantification. The mouse was placed on an XY translation stage (MDrive 17 Plus, Motion Solutions) using a custom-made head holder (*SI Appendix*, Fig. S6*B*). In vivo imaging was performed using a modified commercial two-photon microscope (Ultima, Bruker) with a long working distance objective (TU Plan ELWD 20×, NA 0.4, WD 19 mm, Nikon Instruments Inc.) and a variable-wavelength Ti:sapphire laser with wavelength 920 nm and power 15/40 mW (Chameleon, Coherent Inc.). To observe the cells in the OoC (Fig. 1*H* and *SI Appendix*, Fig. S3*C*), 2.5 mM AM1-43 dye (Biotium) was injected through the round window using a glass pipette. To observe AGs uptake in cochlea, GTTR was systematically injected (i.p. or i.v.). Note that only a part of the HCs in IW area was resolved with GTTR applications (yellow box in *SI Appendix*, Fig. S8*F*) while the dye injection covered all HCs in the area (Fig. 1*H*). The dye injection image allowed for the mouse's head position to be adjusted optimizing the orientation for visualizing the HCs. However, we could not optimize this orientation with GTTR because at the onset of the recording there were no visible HCs.

Z-stack imaging scan with a 2 μm interval was done in Bruker software, Prairie View (Bruker) (Fig. 1*A* and *SI Appendix*, Fig. S8 *B* and *G*). The ranges of z-stack are fully covered not only stria vascularis but also OoC, specifically HC layers. Different laser powers were used (15 mW for stria vascularis and 40 mW for HCs) because the intensity of GTTR fluorescence in stria vascularis and in HCs is quite different. Z-projected image from 50 slices (100 μm depth of stria vascularis region, green box in Fig. 1*A* and *SI Appendix*, Fig. S8*B*) or 30 slices (60 μm depth of OoC, yellow box in Fig. 1*A* and *SI Appendix*, Fig. S8*G*) was used for the quantification of fluorescent intensity. The ROI includes either a stria vascularis or HCs region was selected to be as inclusive as possible was designated in the box (yellow box in *SI Appendix*, Fig. S8 *A* and *F*) (ImageJ Fiji) (68). The averaged GTTR intensity in the ROI in the z-projected image was plotted after subtracting back ground intensity. For averaging purposes, we set the fluorescent intensity to zero when GTTR signals were not detected in HCs. All graphs were made using Origin software (OriginLab).

Immunohistochemistry and Quantification. Cochlea was fixed with 4% PFA/PBS (15710, EMS), and decalcified with 0.5M EDTA (E177, VWR). Whole-mount OoC were dissected and the tectorial membrane was removed. The tissue was permeabilized for 0.5 h in 0.5% Triton X-100/PBS (BP151, Fisher Scientific), and blocked for 2 h in 5% BSA/PBS (BP1600, Fisher Scientific) at room temperature (RT). Staining with primary antibodies was performed overnight at 4 °C and 2 h at 37 °C in the same blocking buffer. After washing with the blocking buffer three times, the tissue was incubated with secondary antibodies and phalloidin diluted in the blocking buffer for 1 h at RT. After washing five times in 1× PBS, the tissue was mounted on slide glass using ProLong Diamond Antifade Mountant with DAPI (P36962, Invitrogen) and saved in the dark at 4 °C. TUNEL assay was performed as recommended in ApopTag plus fluorescein in situ apoptosis detection kit (S7111, EMD Millipore).

For staining HCs, we used primary antibodies against MyosinVIIa (HC marker; 1:500; MYO7A 138-1, DSHB). The secondary antibodies were conjugated with Alexa Fluor 546 (1:500; A10036, Life Technologies). Alexa Fluor 647 conjugated phalloidin staining (F-actin; 1:200; A22287; Invitrogen) was performed with secondary antibody treatment. Z-stack images of the immunostained cochlear tissues were collected by a confocal microscope (LSM700, Zeiss). The number of HCs was counted using ImageJ software.

Statistical Analysis. Statistical analyses were performed using Excel (Microsoft) and Origin (OriginLab). *P* values <0.05 from two-tailed Student's *t* test or ANOVA were considered statistically significant. Change of GTTR intensity over time was fitted by exponential decay function. To compare the fitted data sets, we performed f-test. Error bars represent the standard error of the mean. All statistical tests are listed in *SI Appendix*, Table S1 (*$P < 0.05$; **$P < 0.01$; ***$P < 0.001$; no mark, not significant [$P > 0.05$]).

Data Availability. All study data are included in the article and/or supporting information.

ACKNOWLEDGMENTS. We thank those involved in early stages of development including Nik Blevins, Eduardo Corrales, Jennifer Christy Alyono. We are also grateful to Alan G. Cheng who commented on the manuscript. This project was funded by National Institutes of Health (R01 DC014720 and DC003896-16). Our thanks to philanthropic contributions from the Stanford Initiative to Cure Hearing Loss and the generous donations of the Oberndorf Foundation.

1. R. Tanoshima *et al.*; Canadian Pharmacogenomics Network for Drug Safety Consortium, Analyses of adverse drug reactions-nationwide active surveillance network: Canadian pharmacogenomics network for drug safety database. *J. Clin. Pharmacol.* **59**, 356–363 (2019).
2. World Health Organization, *Critically Important Antimicrobials for Human Medicine* (WHO Document Production Services, 2019).
3. J. Schacht, A. E. Talaska, L. P. Rybak, Cisplatin and aminoglycoside antibiotics: Hearing loss and its prevention. *Anat. Rec. (Hoboken)* **295**, 1837–1850 (2012).
4. T. P. Van Boeckel *et al.*, Global antibiotic consumption 2000 to 2010: An analysis of national pharmaceutical sales data. *Lancet Infect. Dis.* **14**, 742–750 (2014).
5. A. Forge, Outer hair cell loss and supporting cell expansion following chronic gentamicin treatment. *Hear. Res.* **19**, 171–182 (1985).
6. J. O. Pickles, *An Introduction to the Physiology of Hearing* (Emerald Group Publishing Limited, 2008).
7. O. Sterkers, E. Ferrary, C. Amiel, Inter- and intracompartmental osmotic gradients within the rat cochlea. *Am. J. Physiol.* **247**, F602–F606 (1984).
8. O. Sterkers, E. Ferrary, C. Amiel, Production of inner ear fluids. *Physiol. Rev.* **68**, 1083–1128 (1988).
9. R. Patuzzi, Ion flow in cochlear hair cells and the regulation of hearing sensitivity. *Hear. Res.* **280**, 3–20 (2011).
10. Y. Raphael, R. A. Altschuler, Structure and innervation of the cochlea. *Brain Res. Bull.* **60**, 397–422 (2003).
11. G. D. Housley, D. Greenwood, J. F. Ashmore, Localization of cholinergic and purinergic receptors on outer hair cells isolated from the guinea-pig cochlea. *Proc. Biol. Sci.* **249**, 265–273 (1992).
12. G. D. Housley *et al.*, Expression of the P2X(2) receptor subunit of the ATP-gated ion channel in the cochlea: Implications for sound transduction and auditory neurotransmission. *J. Neurosci.* **19**, 8377–8388 (1999).
13. R. Fettiplace, Hair cell transduction, tuning, and synaptic transmission in the mammalian cochlea. *Compr. Physiol.* **7**, 1197–1227 (2017).
14. Q. Wang, P. S. Steyger, Trafficking of systemic fluorescent gentamicin into the cochlea and hair cells. *J. Assoc. Res. Otolaryngol.* **10**, 205–219 (2009).
15. C. F. Dai, D. Mangiardi, D. A. Cotanche, P. S. Steyger, Uptake of fluorescent gentamicin by vertebrate sensory cells in vivo. *Hear. Res.* **213**, 64–78 (2006).
16. S. Imamura, J. C. Adams, Distribution of gentamicin in the guinea pig inner ear after local or systemic application. *J. Assoc. Res. Otolaryngol.* **4**, 176–195 (2003).
17. M. E. Huth, A. J. Ricci, A. G. Cheng, Mechanisms of aminoglycoside ototoxicity and targets of hair cell protection. *Int. J. Otolaryngol.* **2011**, 937861 (2011).
18. H. Li, P. S. Steyger, Systemic aminoglycosides are trafficked via endolymph into cochlear hair cells. *Sci. Rep.* **1**, 159 (2011).
19. A. Alharazneh *et al.*, Functional hair cell mechanotransducer channels are required for aminoglycoside ototoxicity. *PLoS One* **6**, e22347 (2011).
20. W. Marcotti, S. M. van Netten, C. J. Kros, The aminoglycoside antibiotic dihydrostreptomycin rapidly enters mouse outer hair cells through the mechano-electrical transducer channels. *J. Physiol.* **567**, 505–521 (2005).
21. Y. Kawashima *et al.*, Mechanotransduction in mouse inner ear hair cells requires transmembrane channel-like genes. *J. Clin. Invest.* **121**, 4796–4809 (2011).
22. A. Makabe *et al.*, Systemic fluorescent gentamicin enters neonatal mouse hair cells predominantly through sensory mechanoelectrical transduction channels. *J. Assoc. Res. Otolaryngol.* **21**, 137–149 (2020).
23. M. Beurg *et al.*, Variable number of TMC1-dependent mechanotransducer channels underlie tonotopic conductance gradients in the cochlea. *Nat. Commun.* **9**, 2185 (2018).
24. M. E. Huth *et al.*, Designer aminoglycosides prevent cochlear hair cell loss and hearing loss. *J. Clin. Invest.* **125**, 583–592 (2015).
25. T. Karasawa, Q. Wang, Y. Fu, D. M. Cohen, P. S. Steyger, TRPV4 enhances the cellular uptake of aminoglycoside antibiotics. *J. Cell Sci.* **121**, 2871–2879 (2008).
26. R. S. Stepanyan *et al.*, TRPA1-mediated accumulation of aminoglycosides in mouse cochlear outer hair cells. *J. Assoc. Res. Otolaryngol.* **12**, 729–740 (2011).

27. E. Hashino, M. Shero, Endocytosis of aminoglycoside antibiotics in sensory hair cells. *Brain Res.* **704**, 135–140 (1995).
28. S. C. Y. Lin, P. R. Thorne, G. D. Housley, S. M. Vlajkovic, Purinergic signaling and aminoglycoside ototoxicity: The opposing roles of P1 (adenosine) and P2 (ATP) receptors on cochlear hair cell survival. *Front. Cell. Neurosci.* **13**, 207 (2019).
29. H. E. Farris, C. L. LeBlanc, J. Goswami, A. J. Ricci, Probing the pore of the auditory hair cell mechanotransducer channel in turtle. *J. Physiol.* **558**, 769–792 (2004).
30. Y. Karashima *et al.*, Agonist-induced changes in Ca(2+) permeation through the nociceptor cation channel TRPA1. *Biophys. J.* **98**, 773–783 (2010).
31. A. Jara-Oseguera, I. Llorente, T. Rosenbaum, L. D. Islas, Properties of the inner pore region of TRPV1 channels revealed by block with quaternary ammoniums. *J. Gen. Physiol.* **132**, 547–562 (2008).
32. M. Jiang, T. Karasawa, P. S. Steyger, Aminoglycoside-induced cochleotoxicity: A review. *Front. Cell. Neurosci.* **11**, 308 (2017).
33. M. E. O'Sullivan *et al.*, Towards the prevention of aminoglycoside-related hearing loss. *Front. Cell. Neurosci.* **11**, 325 (2017).
34. S. R. Kitcher *et al.*, ORC-13661 protects sensory hair cells from aminoglycoside and cisplatin ototoxicity. *JCI Insight* **4**, e126764 (2019).
35. E. J. Kenyon *et al.*, Identification of a series of hair-cell MET channel blockers that protect against aminoglycoside-induced ototoxicity. *JCI Insight* **6**, 145704 (2021).
36. N. K. Kirkwood *et al.*, d-Tubocurarine and berbamine: Alkaloids that are permeant blockers of the hair cell's mechano-electrical transducer channel and protect from aminoglycoside toxicity. *Front. Cell. Neurosci.* **11**, 262 (2017).
37. Y. Dong, D. Liu, Y. Hu, X. Ma, NaHS protects cochlear hair cells from gentamicin-induced ototoxicity by inhibiting the mitochondrial apoptosis pathway. *PLoS One* **10**, e0136051 (2015).
38. Y. Hirose *et al.*, Quercetin protects against hair cell loss in the zebrafish lateral line and guinea pig cochlea. *Hear. Res.* **342**, 80–85 (2016).
39. Y. R. Kim *et al.*, Galangin prevents aminoglycoside-induced ototoxicity by decreasing mitochondrial production of reactive oxygen species in mouse cochlear cultures. *Toxicol. Lett.* **245**, 78–85 (2016).
40. H. Y. Lee *et al.*, Noninvasive in vivo imaging reveals differences between tectorial membrane and basilar membrane traveling waves in the mouse cochlea. *Proc. Natl. Acad. Sci. U.S.A.* **112**, 3128–3133 (2015).
41. J. Kim, A. Xia, N. Grillet, B. E. Applegate, J. S. Oghalai, Osmotic stabilization prevents cochlear synaptopathy after blast trauma. *Proc. Natl. Acad. Sci. U.S.A.* **115**, E4853–E4860 (2018).
42. J. C. Alyono, C. E. Corrales, M. E. Huth, N. H. Blevins, A. J. Ricci, Development and characterization of chemical cochleostomy in the Guinea pig. *Otolaryngol. Head Neck Surg.* **152**, 1113–1118 (2015).
43. M. J. McGinley, M. C. Liberman, R. Bal, D. Oertel, Generating synchrony from the asynchronous: Compensation for cochlear traveling wave delays by the dendrites of individual brainstem neurons. *J. Neurosci.* **32**, 9301–9311 (2012).
44. D. F. Marker, M. E. Tremblay, S. M. Lu, A. K. Majewska, H. A. Gelbard, A thin-skull window technique for chronic two-photon in vivo imaging of murine microglia in models of neuroinflammation. *J. Vis. Exp.* **43**, 2059 (2010).
45. C. D. Steel, A. L. Stephens, S. M. Hahto, S. J. Singletary, R. P. Ciavarra, Comparison of the lateral tail vein and the retro-orbital venous sinus as routes of intravenous drug delivery in a transgenic mouse model. *Lab Anim. (NY)* **37**, 26–32 (2008).
46. C. Askew *et al.*, Tmc gene therapy restores auditory function in deaf mice. *Sci. Transl. Med.* **7**, 295ra108 (2015).
47. R. Dagil, C. O'Shea, A. Nykjaer, A. M. J. J. Bonvin, B. B. Kragelund, Gentamicin binds to the megalin receptor as a competitive inhibitor using the common ligand binding motif of complement type repeats: insight from the nmr structure of the 10th complement type repeat domain alone and in complex with gentamicin. *J. Biol. Chem.* **288**, 4424–4435 (2013).
48. J. Tauris *et al.*, Cubilin and megalin co-localize in the neonatal inner ear. *Audiol. Neurotol.* **14**, 267–278 (2009).
49. Y. Hori *et al.*, Megalin blockade with cilastatin suppresses drug-induced nephrotoxicity. *J. Am. Soc. Nephrol.* **28**, 1783–1791 (2017).
50. D. Ding *et al.*, Ototoxic effects and mechanisms of loop diuretics. *J. Otol.* **11**, 145–156 (2016).
51. G. Al-Malky, S. J. Dawson, T. Sirimanna, E. Bagkeris, R. Suri, High-frequency audiometry reveals high prevalence of aminoglycoside ototoxicity in children with cystic fibrosis. *J. Cyst. Fibros.* **14**, 248–254 (2015).
52. A. C. Garinis *et al.*, The cumulative effects of intravenous antibiotic treatments on hearing in patients with cystic fibrosis. *J. Cyst. Fibros.* **16**, 401–409 (2017).
53. A. L. Nuttall, D. F. Dolan, G. Avinash, Laser Doppler velocimetry of basilar membrane vibration. *Hear. Res.* **51**, 203–213 (1991).
54. M. A. Ruggero, N. C. Rich, Application of a commercially-manufactured Doppler-shift laser velocimeter to the measurement of basilar-membrane vibration. *Hear. Res.* **51**, 215–230 (1991).
55. T. Ren, Longitudinal pattern of basilar membrane vibration in the sensitive cochlea. *Proc. Natl. Acad. Sci. U.S.A.* **99**, 17101–17106 (2002).
56. T. Ren, Reverse propagation of sound in the gerbil cochlea. *Nat. Neurosci.* **7**, 333–334 (2004).
57. W. Dong, E. S. Olson, Detection of cochlear amplification and its activation. *Biophys. J.* **105**, 1067–1078 (2013).
58. P. Dallos, Response characteristics of mammalian cochlear hair cells. *J. Neurosci.* **5**, 1591–1608 (1985).
59. I. J. Russell, P. M. Sellick, Low-frequency characteristics of intracellularly recorded receptor potentials in guinea-pig cochlear hair cells. *J. Physiol.* **338**, 179–206 (1983).
60. M. C. Liberman, Auditory-nerve response from cats raised in a low-noise chamber. *J. Acoust. Soc. Am.* **63**, 442–455 (1978).
61. H. Y. Lee *et al.*, Two-dimensional cochlear micromechanics measured in vivo demonstrate radial tuning within the mouse organ of Corti. *J. Neurosci.* **36**, 8160–8173 (2016).
62. R. K. Wang, A. L. Nuttall, Phase-sensitive optical coherence tomography imaging of the tissue motion within the organ of Corti at a subnanometer scale: A preliminary study. *J. Biomed. Opt.* **15**, 056005 (2010).
63. M. O'Reilly *et al.*, Design, synthesis, and biological evaluation of a new series of carvedilol derivatives that protect sensory hair cells from aminoglycoside-induced damage by blocking the mechanoelectrical transducer channel. *J. Med. Chem.* **62**, 5312–5329 (2019).
64. D. Dulon, H. Hiel, C. Aurousseau, J. P. Erre, J. M. Aran, Pharmacokinetics of gentamicin in the sensory hair cells of the organ of Corti: Rapid uptake and long term persistence. *C. R. Acad. Sci. III* **316**, 682–687 (1993).
65. M. E. O'Sullivan *et al.*, Dissociating antibacterial from ototoxic effects of gentamicin C-subtypes. *Proc. Natl. Acad. Sci. U.S.A.* **117**, 32423–32432 (2020).
66. B. Pan, J. Waguespack, M. E. Schnee, C. LeBlanc, A. J. Ricci, Permeation properties of the hair cell mechanotransducer channel provide insight into its molecular structure. *J. Neurophysiol.* **107**, 2408–2420 (2012).
67. M. Jiang *et al.*, Inflammation up-regulates cochlear expression of TRPV1 to potentiate drug-induced hearing loss. *Sci. Adv.* **5**, eaaw1836 (2019).
68. J. Y. Tinevez *et al.*, TrackMate: An open and extensible platform for single-particle tracking. *Methods* **115**, 80–90 (2017).